"Sol-gel and hydrothermal synthesis of CeO$_2$ NPs: Their physiochemical properties and applications for gas sensor with photocatalytic activities"

Laxmi D. Sonawane [a], Abhinay S. Mandawade [a], Laxman N. Bhoye [a], Huda I. Ahemad [a], Swapnil S. Tayade [a], Yogesh B. Aher [a], Anil B. Gite [a], Latesh K. Nikam [b], Sarika D. Shinde [a], Gotan H. Jain [a], Ganesh E. Patil [a], Mahendra S. Shinde [c],[*]

[a] Dept. Of Physics, SNJB's Arts, Commerce and Science College Chandwad, Nashik 423101, India
[b] Dept. Of Chemistry, PDA's Annasaheb Magar College, Hadapsar, Pune 411028, India
[c] Dept. Of Physics, M.J.M. Arts, Commerce and Science College, Karanjali (Peth), Nashik 422208, India

ARTICLE INFO

ABSTRACT

Cerium dioxide (CeO$_2$) nanoparticles were synthesized through sol–gel and hydrothermal methods, yielding materials with distinct properties. Characterization techniques including Fourier Transform Infrared Spectroscopy (FTIR), Ultraviolet–visible spectroscopy (UV–Vis), X-ray Diffraction (XRD), Raman spectroscopy, Cyclic Voltammetry (CV), Photoluminescence spectra (PL), Field Emission Scanning Electron Microscopy (FESEM), and Transmission Electron Microscopy with Selected Area Electron Diffraction (TEM-SAED) were employed to analyse the synthesized nanoparticles. The FTIR analysis revealed an absorption band at 475 cm^{-1}, while UV–Visible spectroscopy determined band gap energies of 3 eV and 3.16 eV for the sol–gel and hydrothermal methods, respectively. XRD analysis indicated crystalline sizes of 14.57 nm and 17.41 nm for the sol–gel and hydrothermal methods, respectively. Raman spectroscopy demonstrated active peaks at 464 cm^{-1} for the sol–gel method and 463 cm^{-1} for the hydrothermal method. Cyclic Voltammetry showcased different oxidation and reduction peaks, while Photoluminescence spectra provided insights into the excitation spectrum of CeO$_2$ nanoparticles. FESEM and TEM-SAED images revealed nano-sized spherical spongy CeO$_2$ nanoparticles. Furthermore, the synthesized CeO$_2$ nanoparticles exhibited promising photocatalytic degradation activity against methyl blue (MB) dye under sunlight irradiation, with degradation efficiencies of 92 % and 82 % for the sol–gel and hydrothermal methods, respectively. Additionally, gas sensing properties for various gases (ethanol, methanol, CO$_2$, LPG, H$_2$S, and NH$_3$) were evaluated using domestic gas sensor systems, showing potential applicability across a broad temperature range from 50 °C to 350 °C.

1. Introduction

Cerium oxide (CeO$_2$) is an active rare earth oxide stable and good electron acceptor, has excellent biocompatibility with approximately or no toxicity, is not very costly, and is environmentally friendly. Cerium has two oxidation states, tetravalent (Ce^{4+}) and trivalent (Ce^{3+}). Therefore, cerium oxide exists in two different oxides ((Ce$_2$O$_3$ (Ce^{3+}) and CeO$_2$ (Ce^{4+})) depending on the nature of the materials [1]. CeO$_2$ nanoparticles (NPs) have attained significant consideration in nanomedicine and other applications because of their promising use in biosensing [2], antibacterial [3], solar cell [4], corrosion inhibition [5], gas-sensing [6], photocatalytic activity [7], supercapacitor [8], biological sensors [9]. In the field of gas-sensing, because of its good chemical resistance, non-toxicity, safety, and reliability, cerium oxide is an n-type semiconducting and encouraging material used for sensing O$_2$ at high temperatures remaining to its chemical stability and high diffusion co-efficient vacancies and one potential active or additive sensing material for monitoring explosive, poisonous and hazardous gases [10,11]. Such as NH$_3$ [12], H$_2$S [13], CO [14], C$_2$H$_5$OH [15]. Photocatalysis has been considered a green and effective approach to the elimination of environmental pollution [16]. Cerium oxide photocatalysts, including non-metal doping, dye sensitization, metal doping, coupling of semiconductors, and polymer sensitization, are one of the most potential photocatalysts with UV–vis light response due to the rich in oxygen vacancies and are found to have incredible effects in photocatalysis [17,18]. By using synthesized CeO$_2$ NPs, various dyes are used for the
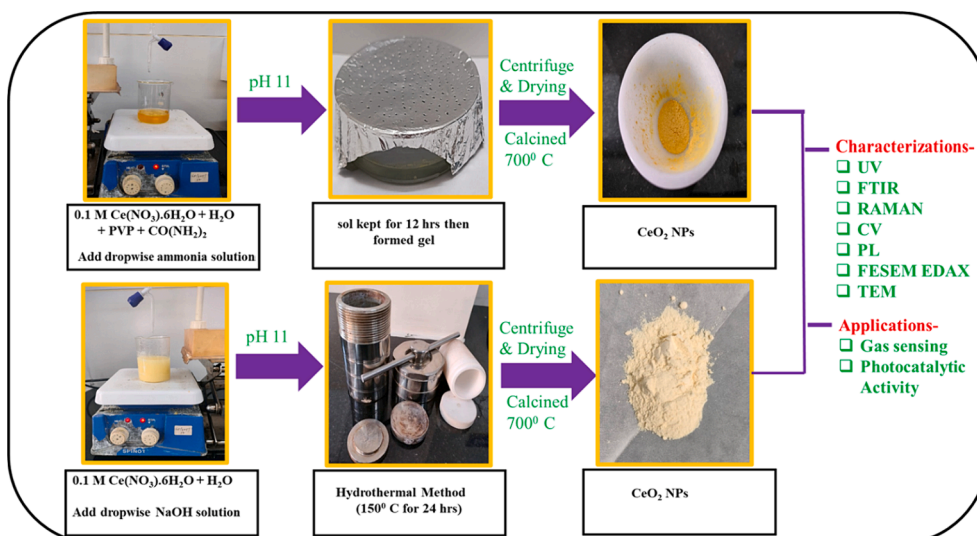

Fig. 1. Schematic representation of synthesized CeO$_2$ NPs.

photocatalytic activity, such as methyl orange (MO) [19], methyl blue (MB) [7], amido black [20], rhodamine B [21], tartrazine [22]. Cerium oxide nanomaterials are synthesized using various methods such as green synthesis [19], co-precipitation [7], chemical bath deposition [23], sol–gel [24], hydrothermal [25], spray pyrolysis [26].

To the best of our knowledge, no report on comparing the effects of synthesis parameters on structural and morphological features of CeO$_2$ NPs synthesized using sol–gel and hydrothermal methods and its resultant impact on optical properties, gas sensing properties, and photocatalytic activities has been published yet [27,28,29]. Hence, to find how chemical synthesis routes sol–gel and hydrothermal methods, control the structure and morphology of the synthesized particles and consequently the optical, gas sensing, and photocatalytic properties, the current study has been conducted.

In the present work, CeO$_2$ NPs were synthesized using sol–gel and hydrothermal methods and analyzed using various characterization techniques, such as XRD, UV–Vis, FT-IR, Raman, CV, PL, FESEM, and TEM-SAED. The synthesized CeO$_2$ NPs by sol–gel method demonstrate outstanding gas sensing response and photocatalytic activity as compared to hydrothermal synthesized NPs when they are exposed to sunlight.

2. Materials and methods

2.1. Materials

All reagents used were of AR Grade. Cerium nitrate (Ce (NO$_3$)$_3$).6H$_2$O) of Sigma Aldrich (99.9 % purity) and Urea CO(NH$_2$)$_2$, Polyvinyl-Pyrolydine (PVP), Ammonia, Ethanol all of Merck Chemical (99.9 % purity) and Sodium Hydroxide (NaOH) of S.D fine (99.9 % purity) make have been used. Fig. 1..

2.2. Methods

2.2.1. Synthesis of CeO$_2$ NPs by sol–gel method

CeO$_2$ NPs were synthesized by the sol–gel method. Cerium precursor (0.1 mol) cerium nitrate (Ce (NO$_3$)$_3$).6H$_2$O), (0.05 mol) Urea CO(NH$_2$)$_2$ and (0.01 mol) Polyvinyl-Pyrolydine (PVP) were dissolved in 100 ml of deionized water. The initial pH was 3.4 acidic solution. This solution was stirred for 30 min. Then, an appropriate amount of ammonia was added dropwise. After stirring for 2 hrs, the color of the solution became purple and gradually changed into a pale-yellow color gel with a final pH of 11. The gel was collected by centrifugation and washed with

ethanol under 11,000 Revolution per Minute (rpm). Finally, the gel was dried at 80 °C for 24 hrs, and the product was collected. The Ce^{3+} was oxidized into Ce^{4+} by O$_2$ under the air atmosphere [24,30]. The product was annealed in a muffle furnace at 700 °C.

2.2.2. Synthesis of CeO$_2$ NPs by hydrothermal method

CeO$_2$ NPs were synthesized by hydrothermal method. Cerium precursor (0.1 mol) cerium nitrate (Ce(NO$_3$)$_3$).6H$_2$O were dissolved in 50 ml of deionized water. The initial pH was 3.2 acidic solution. This solution was stirred for 60 min. Then, an appropriate amount of sodium hydroxide solution was added dropwise and stirred for 3 hrs, and its color became purple and gradually changed into a pale-yellow color solution with a final pH of 11. The suspension was transferred to 100 ml. Teflon-lined stainless-steel autoclave sealed and had a hydrothermal reaction at 150 °C for 24 hrs. The solution was collected by centrifugation and washed with methanol under the conditions of 11000 rpm [25 31,32]. Finally, the solution was dried at 80 °C for 24 hrs, and the product was collected and formed CeO$_2$ NPs. The CeO$_2$ NPs were annealed in a muffle furnace at 700 °C.

2.3. Characterization

The synthesized nanomaterial is characterized by X-ray Diffraction (XRD) (X-ray Source-Cu K alpha, Model-Miniflex 600, and make-Rigaku). The band gap energy was found by UV–Vis diffuse reflectance Spectrophotometer (model-2600 and Make-Shimadzu). Chemical bond interpretation and functional group detection by Fourier transform infrared spectrometry (FT-IR) model-IR Affinity-1 with diamond ATR and make Shimadzu) and Raman spectra (Invia Renishaw micro-Raman spectrophotometer). Morphological study by Field Emission Scanning Electron Microscopy (FESEM) (Carl Zeiss Model Supra 55 Germany). PL spectra study by JASCO Spectroflorometer (Model FP-8300 WRE) and TEM analysis done by JEOL JEM 2100 plus.

2.4. Photocatalytic experiments

The synthesized CeO$_2$-NPs by sol–gel and hydrothermal methods have been employed for photocatalytic degradation of MB dye under direct sunlight irradiation in the month of May 2023 between 11.00 a.m. to 2.00p.m. The average intensity of sunlight was observed to be in the range of 810 W/m^2 measured by using a sun meter (Make Solaron, Model-DSM 01). The 10 mg of catalyst (synthesized CeO$_2$ sNPs by sol--gel and hydrothermal method) was added into 100 ml, 10 ppm MB
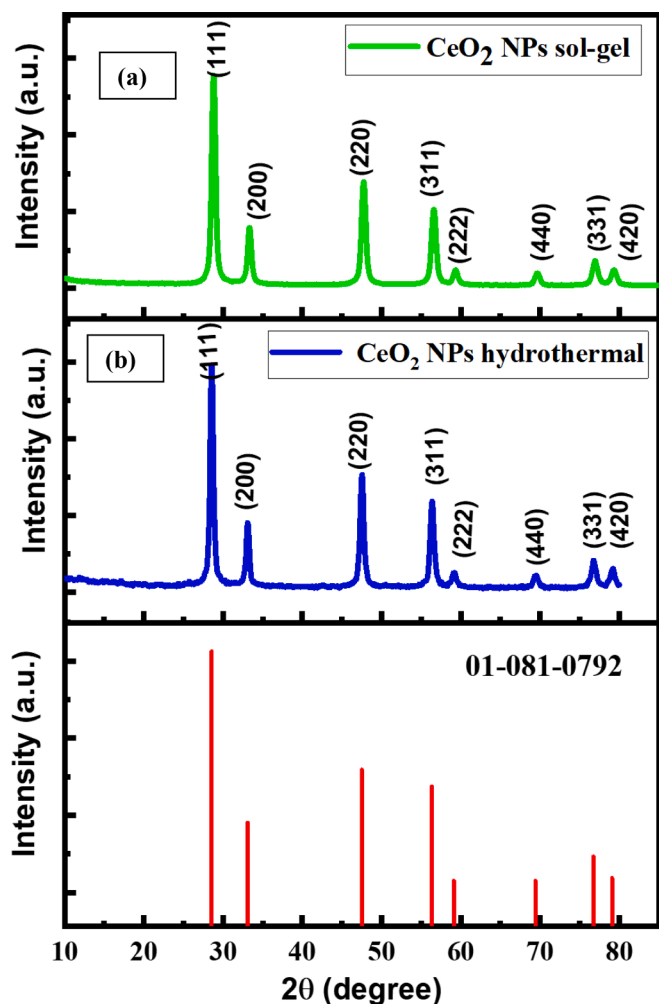
Fig. 2. X-ray diffraction pattern of CeO_2 NPs for a) sol–gel and b) hydrothermal Method.

solution separately in 100 ml of distilled water, and 10 ppm MB dye aqueous solution was magnetically stirred in the dark for 30 min to achieve max adsorption [33]. Then, the suspension was kept under sunlight, and 10 ml volume was removed in a test tube covered with black paper every 30 min. The gradual color change from blue to colorless was observed during irradiation of sunlight. The Collected solutions were centrifuged to remove the catalyst. Absorption of the samples collected was measured using a UV–vis spectrophotometer The percentage of MB degradation was calculated by following equation [7,34].

$$\text{Photocatalytic degradation} (\%) = A_0 - A_t / A_0 \times 100 \qquad (1)$$

where, A_0 is initial in absorbance and
A_t is absorbance at time t.

2.5. Gas sensing

The gas sensing performance of CeO_2 NPs was studied by preparing their thick films by using the screen-printing method. The response of the sensor was calculated by the following relation [12].

$$S \% = R_a - R_g / R_a \times 100 \qquad (2)$$

where R_a is the resistance of the air
R_g is the resistance in the presence of gas.
For sensing measurements, liquid ammonia was used to produce ammonia gas. The part per million (ppm) concentration of ammonia was calculated by static distribution liquid gas using the following relation [35].

$$\text{Concentration} (\text{ppm}) = 22.4 \, \rho T \, V' / 27 MV \, x1000 \qquad (3)$$

where,
ρ - density of liquid (g/mL), V'- volume of liquid (μL), T- testing temperature (K),
M- molecular weight of gas (g/mol), V- volume of the testing chamber.

3. Results and discussion

3.1. Powder X-ray diffraction studies

The XRD pattern of synthesized CeO_2 NPs obtained is shown in Fig. 2 (a,b) XRD pattern of CeO_2 by sol–gel and hydrothermal method the diffraction intensities were recorded from 20° to 80° in Fig. 2(a) consequential of crystals planes at 2θ of 28.68°, 33.34°, 47.60°, 56.40°, 59.26°, 69.61°, 76.86°, 79.20° which correspond to crystal planes (111), (200), (220), (311), (222), (400), (331), (420) and Fig. 2(b) for the hydrothermal method 28.43°, 33.09°, 47.33°, 56.42°, 59.00°, 69.36°, 76.86°, 79.20° correspond to crystal planes (111), (200),
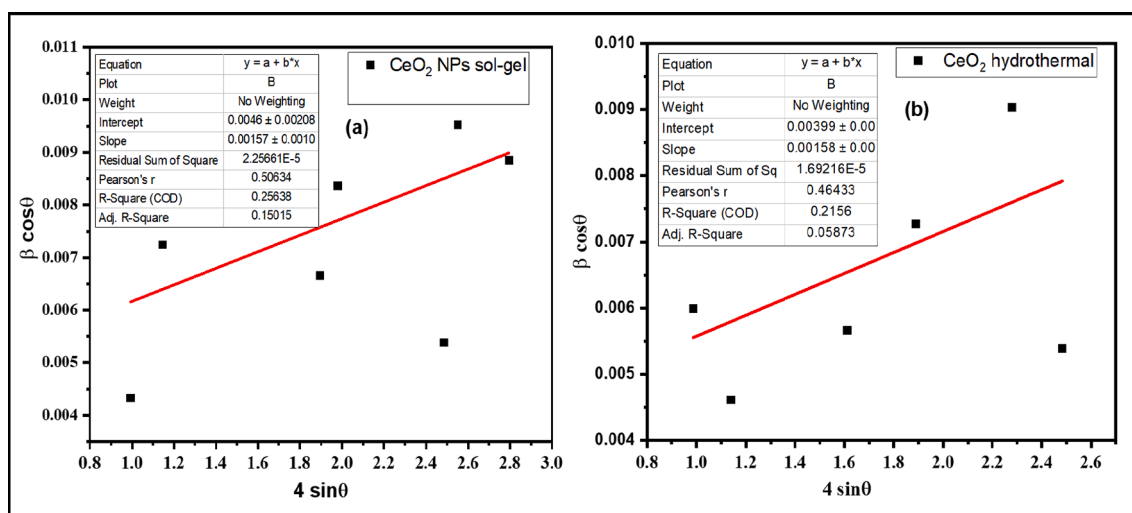

Fig. 3. W-H plots of CeO_2 NPs by a) sol–gel and b) hydrothermal method.
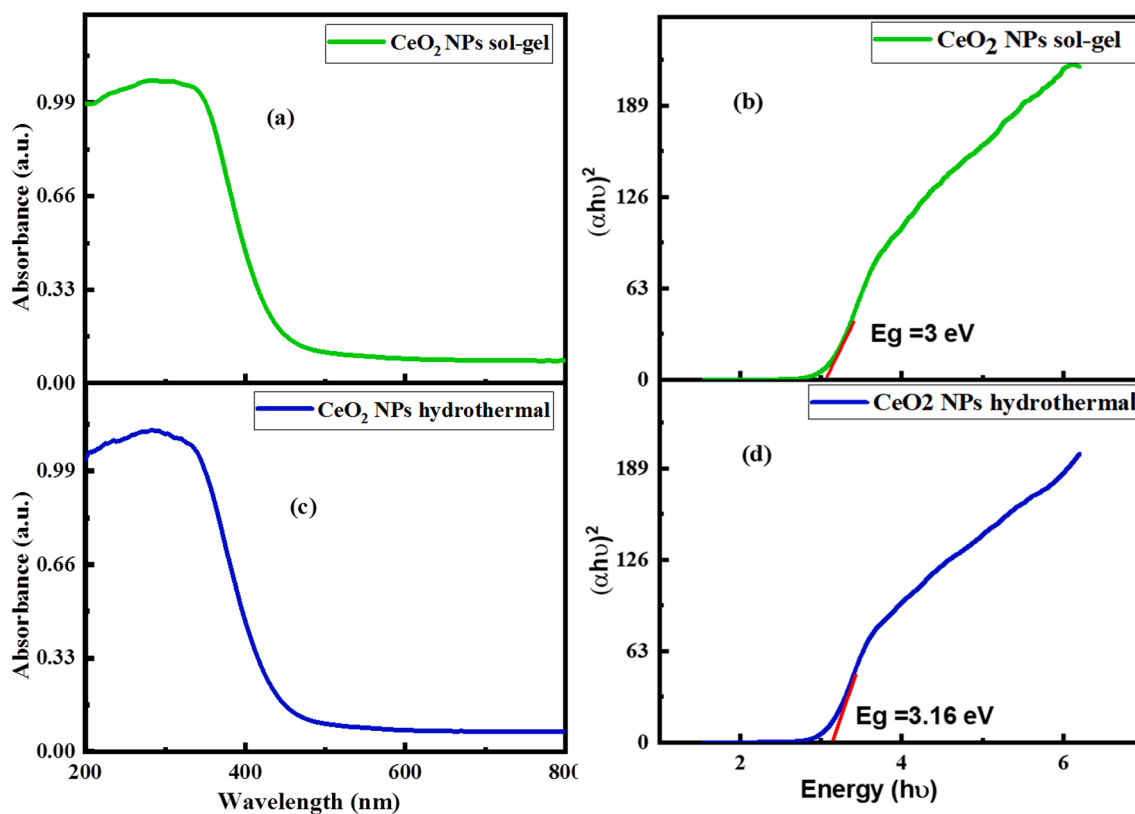
Fig. 4. UV–Vis DRS spectrum and Tauc plot of CeO$_2$ NPs for a) sol–gel and b) Hydrothermal method.

(2 2 0), (3 1 1), (2 2 2), (4 0 0), (3 3 1), (4 2 0) and XRD pattern of CeO2 synthesized by Hydrothermal and Sol Gel method matches exactly with JCPDS File No. 01–081-0792 which confirms cubic phase (fcc) with specific group Fm3m and lattice parameters a = 5.4142 A°, V = 158.55

Fig. 5. (a,b) FT-IR spectra of CeO$_2$ NPs by a) sol–gel and b) hydrothermal method.

(A°)^3, Z = 4 and calculated density (d) = 7.21 g/cm^3 [23].

[a]. The average crystallite size of synthesized CeO$_2$ was calculated by using Debye- Scherer's formula and the Williamson–Hall (W–H) method [19 36].

I Debye- Scherer's formula

$$D = 0.9\lambda/\beta\cos\theta \tag{4}$$

where D is the crystallite size, λ- is the X-ray wavelength of CuKα radiation (0.154 nm), β-is the full-width half maximum (FWHM) of the peak, θ is the diffraction peak angle. The average crystalline size of the synthesized CeO$_2$ NPs by sol–gel method was 14.57 nm and by hydrothermal method 17.41 nm. No other impurity peak is present, which represents the purity of the CeO$_2$ NPs by sol–gel and hydrothermal method [22].

ii Williamson–Hall (W–H) method

The total peak broadening is the sum of the contributions of the crystal size and the strain present in the material. From Fig. 3 The W–H equation for the uniform determination model is given by [37].

$$\beta(hkl)\cos\theta(hkl) = k \times \lambda/D_v 4\varepsilon \sin\theta(hkl) \tag{5}$$

where, β$_{(hkl)}$ s is the FWHM, θ is Bragg's diffraction angle, k is the shape factor, λ is the wavelength of radiation, D$_v$ is the volume-weighted crystallite size, and ε is the lattice strain. The crystalline size is obtained from the intercept value of the plot [38]. The crystalline size of the synthesized CeO$_2$ NPs by sol–gel was found to be 30.14 nm and by hydrothermal method 34.75 nm.

[b]. The lattice parameter calculated from the (1 1 1) reflection plane of the synthesized CeO$_2$ NPs is calculated by the formula [19].

$$a = d_{hkl}\sqrt{h^2 + K^2 + l^2} \tag{6}$$

where d is the spacing and (h k l) are the miller indices, the calculated lattice parameters of synthesized CeO$_2$ NPs by sol–gel method and
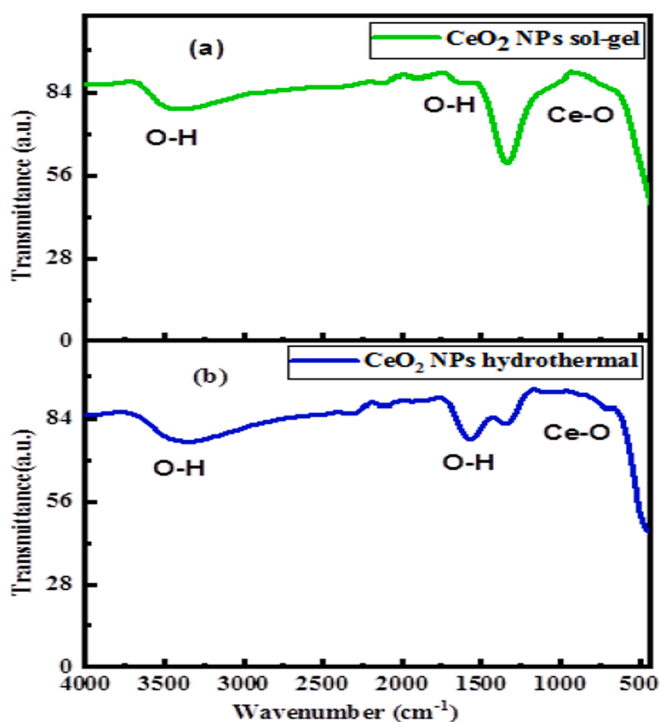
Table 1

Assignments for absorption bands/peaks of FTIR spectrum of CeO$_2$ NPs by sol–gel and hydrothermal method.

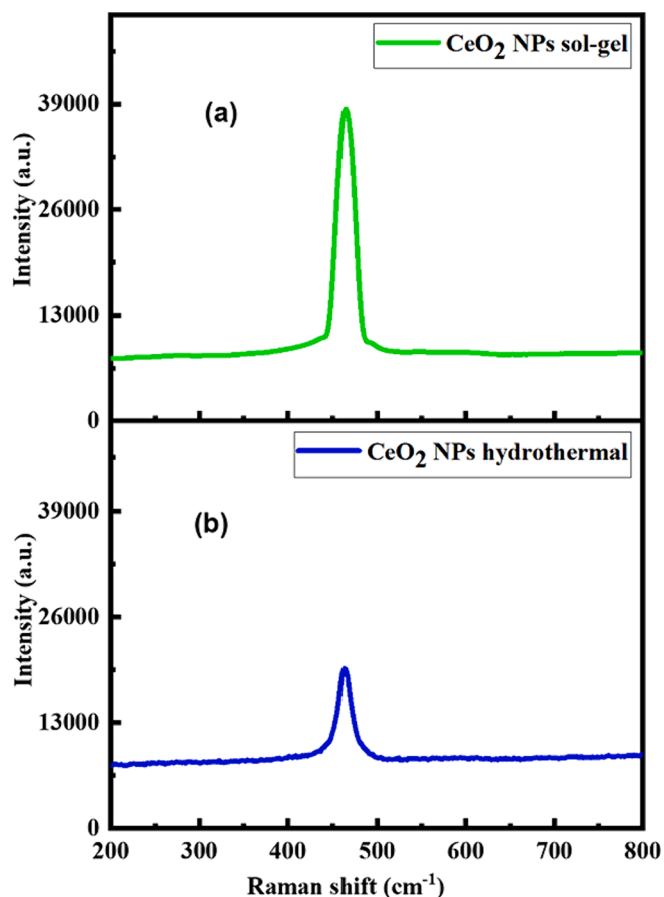| Bands/peaks (cm^{-1})	Assignments
475	strong stretching vibration of Ce-O
848	Ce-O bond
3376	O–H stretching vibration mode
1555	O–H bending vibration mode
1300	Presence of residual matter

Fig. 6. (a,b) Raman spectra of CeO$_2$ NPs by a) sol–gel and b) hydrothermal Method.

hydrothermal method a = 0.5254 nm due to the presence of oxygen deficiency in CeO$_2$ NPs and $\alpha = \beta = \gamma = 90°$ [39].

3.2. Uv–visible DRS analysis

Fig. 4(a–d) gives the UV–visible Diffused Reflectance Spectra of the synthesized CeO$_2$ NPs by sol–gel and hydrothermal method. The UV–Vis absorption edge provides a desirable estimation of the band gap energy of synthesised material. From absorption data, the band gap energy (Eg) of the prepared samples was calculated using Tauc's equation as given below [3].

$$(\alpha h\vartheta)1/n = A(h\vartheta - E_g) \tag{7}$$

Where α is the absorption coefficient, and n is a constant that depends on the transition probability. Fig. 4 (b,d) shows the variation of $(\alpha h\upsilon)^2$ vs energy (hυ). Putting energy axis x = 0, the band gap energy Eg can be deduced by generalizing the linear portion of the graph [40]. The energy band gap CeO$_2$ NPs synthesized by the sol–gel was found to be 3 eV, and
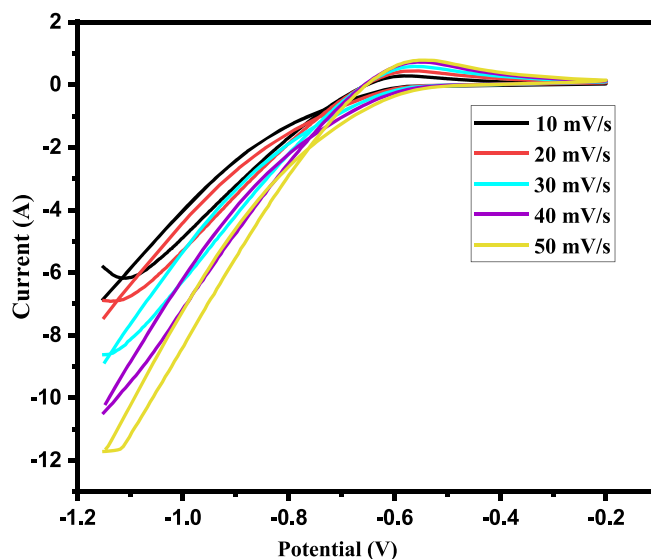

Fig. 7. Cyclic voltammogram of CeO$_2$ NPs.

by the hydrothermal method, the band gap energy was found to be 3.16 eV.

3.3. Fourier-transform infrared spectroscopy

It is well-accepted that FT-IR spectra can be used as an essential analytical tool to identify the functional group present in the materials. Fig. 5(a,b) the FTIR spectrum of CeO$_2$ NPs synthesized by the sol–gel and hydrothermal method exhibited the absorption band at around 475 cm^{-1}, which is assigned to the strong stretching vibration of Ce-O, The band at 848 cm^{-1} corresponds to metal–oxygen bond, Small peaks at around 3376 cm^{-1} and 1555 cm$^{-1,}$ which are related to the O–H stretching vibration mode and bending vibration of associated water, respectively which indicates the presence of residual water [15]. In addition, band around 1300 cm^{-1} has been observed in CeO$_2$ synthesized by the hydrothermal method indicating presence of residual organic matter on the surface. Table 1 shows absorption peaks of FTIR spectrum of CeO2 NPs by sol–gel and hydrothermal method.

3.4. Raman spectra studies

The raman spectrum of CeO$_2$ NPs synthesized by sol–gel and hydrothermal method is shown in Fig. 6(a,b) The raman shift range is from 200 to 800 cm^{-1}. For the CeO$_2$ NPs by sol–gel method, an active raman peak with a strong and broad intensity mode was formed at 464 cm^{-1} and for the hydrothermal method, it is about 463 cm^{-1}. In this case, F$_2$g is the lattice mode of the spectra, and this peak is directly linked to the symmetrical stretching mode of the Ce–O bond, confirming the formation of a fluorite-type structure. This vibration is extremely sensitive to the calcination temperature-induced instability in the oxygen lattice sites [41,42].

3.5. Cyclic voltammetry

From Fig. 7. In cyclic voltammetry, the sweep rate of 10 to 50 mV/s was used, the potential range was altered from −1.2 V to −0.1 V, and the oxidation and reduction peaks were observed at a potential range of −0.55 V The sweep rate 10 mV/s, 20 mV/s, 30 mV/s, 40 mV/s, 50 mV/s corresponding to the data sampling time 166 ms, 103 ms, 78 ms, 64 ms, 54 ms. As the sweep rate increases, sampling time decreases [43,44].
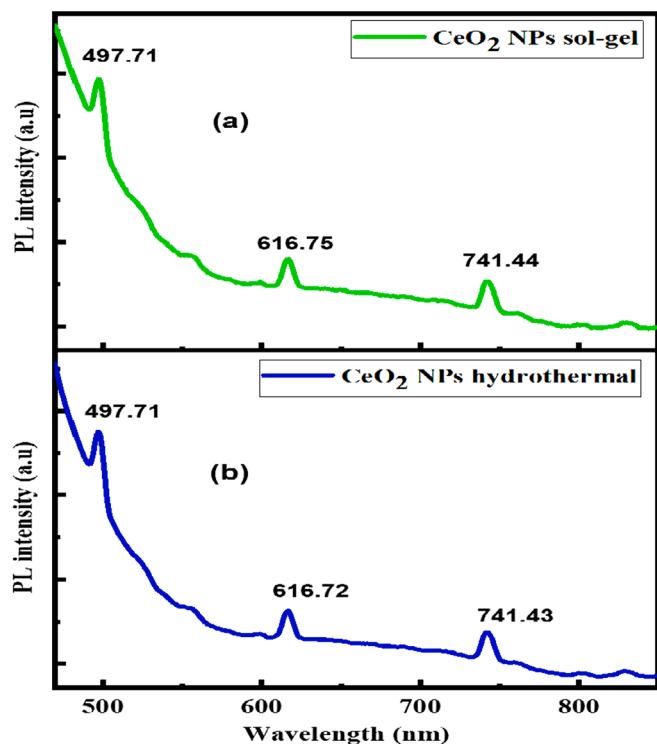
Fig. 8. PL of CeO$_2$ NP by (a) sol–gel and (b) hydrothermal method.

3.6. Photoluminescence spectra (PL)

In Fig. 8(a,b), the excitation spectrum of CeO$_2$ NPs formed through (a) sol–gel and (b) hydrothermal methods is presented. The corresponding photoluminescence (PL) spectrum of the as-formed CeO$_2$ NPs is also depicted. Notably, the PL spectrum reveals three predominant emission peaks: a substantial band at 616 nm, a minor band at 741 nm, and faint blue bands at 497 nm. The concentration of CeO$_2$ NPs has been identified as a factor influencing the blue shift peak in the PL spectrum. To elucidate these observations, it is proposed that the charge transfer from the 4f band to the valence band of CeO$_2$ NPs plays a crucial role. The diminished intensity of the green emission peak in this sample is likely attributed to the low density of oxygen vacancies during the sol–gel and hydrothermal fabrication processes. Additionally, the subtle blue and weak blue-green emissions in this sample may be linked to surface defects in the CeO$_2$ NPs [45].

3.7. FESEM and EDAX analysis

Fig. 9(a,b,c,d) and Fig. 10(a,b,c,d) shows the FESEM image with EDAX spectra and compositional data of CeO$_2$ NPs synthesized by sol–gel and hydrothermal method respectively. Fig. 9(a,b) and Fig. 10(a,b) show nanosized spherical spongy CeO$_2$ nanoparticles with irregular clusters with porous nature [46]. Fig. 9(c) and Fig. 10(c) EDAX spectrum shows only Ce and O components without impurities. Fig. 9(d) and Fig. 10(d) show the compositional data of Ce and O [47,18,48]. It was found that CeO$_2$ NPs by sol–gel are more oxygen-deficient than the hydrothermal method. Oxygen deficiency is important in the gas-sensing mechanism.
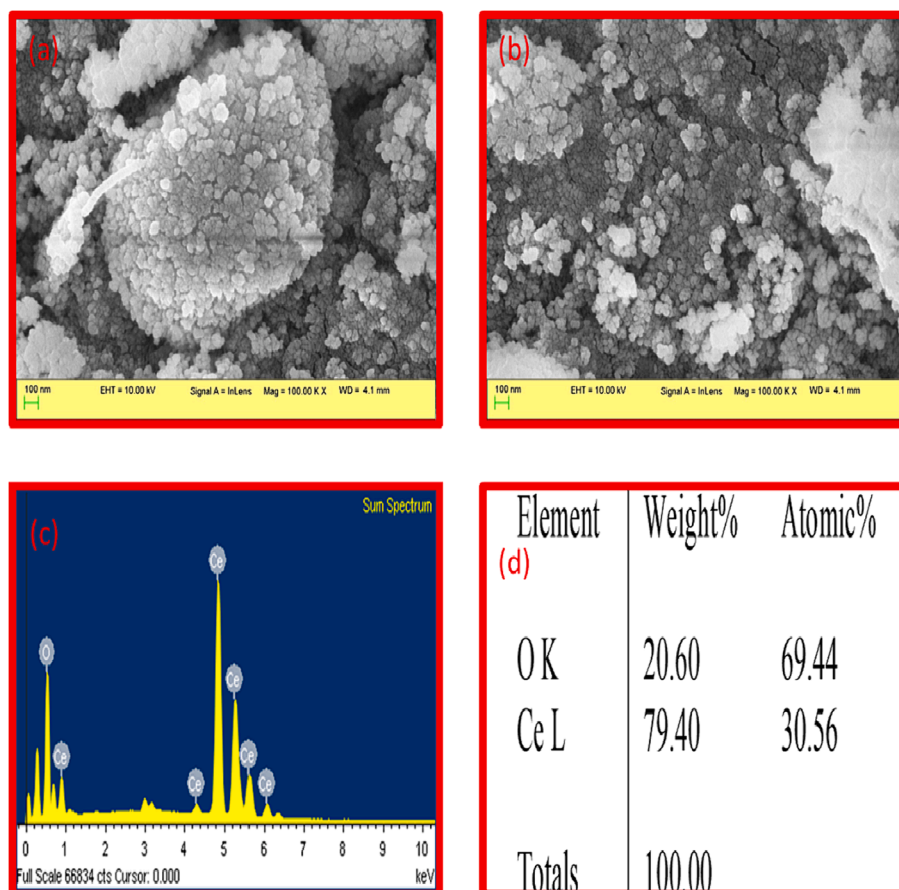

Fig. 9. (a,b,c,d) FESEM images (a&b), EDAX spectrum (c), and compositional data (d) of CeO$_2$ NPs by sol–gel method.
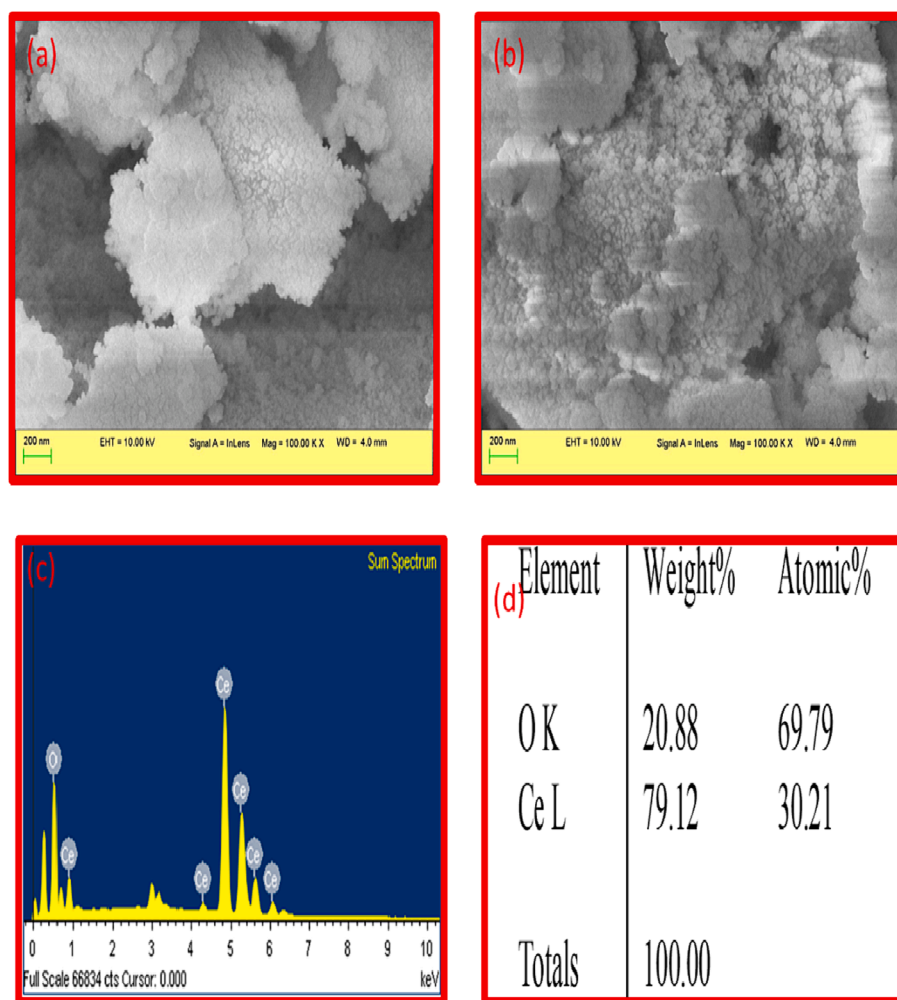
Fig. 10. (a,b,c,d) The FESEM images (a&b), EDAX spectrum (c), and compositional data (d) of CeO_2 NPs by hydrothermal method.

3.8. TEM –SAED

The image is presented in Fig. 11(a,b,c,d,e,f,g,h) shows the TEM analysis, the size distribution, the interplanar distance measurement, and the SAED of the sol–gel and hydrothermal method. Fig. 11(a,b) shows the morphology of the CeO_2 NP spherical shape. Furthermore, the CeO_2 NPs by sol–gel smallest diameters and hydrothermal method largest diameters. To further analyse the morphology of the nanoparticles. The size distribution is shown in Fig. 11(c,d) the CeO_2 NPs by sol–gel and hydrothermal samples have an average particle size of 15.96 and 17 nm and respectively [49].

The Fig. 11(e,f) shown on a smaller scale (10 nm). In these images, both the fingerprints of CeO_2 NPs and their similar spherical shape can be observed and the interplanar distance of the samples was calculated, where all two showed to be 0.318 nm and 0.315 nm typical distance from these NPs. this distance corresponds to the (1 1 1) plane, being verified using the XRD [50].

Finally, the images Fig. 11(g,h) show the SAED diffraction patterns, presenting the ring (1, 2, 3, 4, 5, 6, 7, 8) which based on the JCPDS file no. 01–081-0792 corresponds to the cubic crystal structure of CeO_2 NPs by sol–gel and hydrothermal method [51].

3.9. Photocatalytic studies

CeO_2 is having high refractive index, optical transparency in visible region, oxygen storage capacity, chemical reactivity as well as absorbs larger fraction solar energy spectrum. These factors makes CeO_2 as a good photo catalyst for various processes. It's photocatalytic activity can be improved by changes in morphology, doping, coupling with other semiconductors and combination with carbon supporting material. Herein we have attempted to improve photocatalytic activity on the basis of morphology [52].

The rise of environmental pollution at an enormous level due to emissions of toxic pollutants by dissimilar industries caused numerous hazardous health effect[53]. Among these pollutants, organic compounds such as azo dyes (MB) have become very dangerous due to their harmful impact on the environment and human health [7,54]. Therefore, removing MB dye from effluent is essential to protect the environment.

The photocatalytic activity of the synthesized CeO_2 NPs by the sol–gel and hydrothermal methods was studied for the degradation of MB dye under sunlight irradiation [19]. In Fig. 12(a,b) The absorption spectra of the MB solution has been monitored and recorded at regular intervals (0, 30, 60, 90, 120, 150, 180 and 210 min). The rate of degradation studied in terms of decrease in absorption of MB solution at $\lambda max = 664$ nm.

3.9.1. Mechanism of photocatalytic decay

The mechanism of photocatalytic reaction catalysed by synthesized CeO_2-NPs by the sol–gel and hydrothermal method is shown in Fig. 12(f) When the CeO_2-NPs are radiated by sunlight, the electrons (e⁻) from the valence band transfer to the conduction band by absorbing the energy, and the electron (e^-_{cb}) reacts with absorbed molecular O_2 reducing superoxide radical O_2^-. The holes (h^+_{vb}) can produce OH• free radicals and
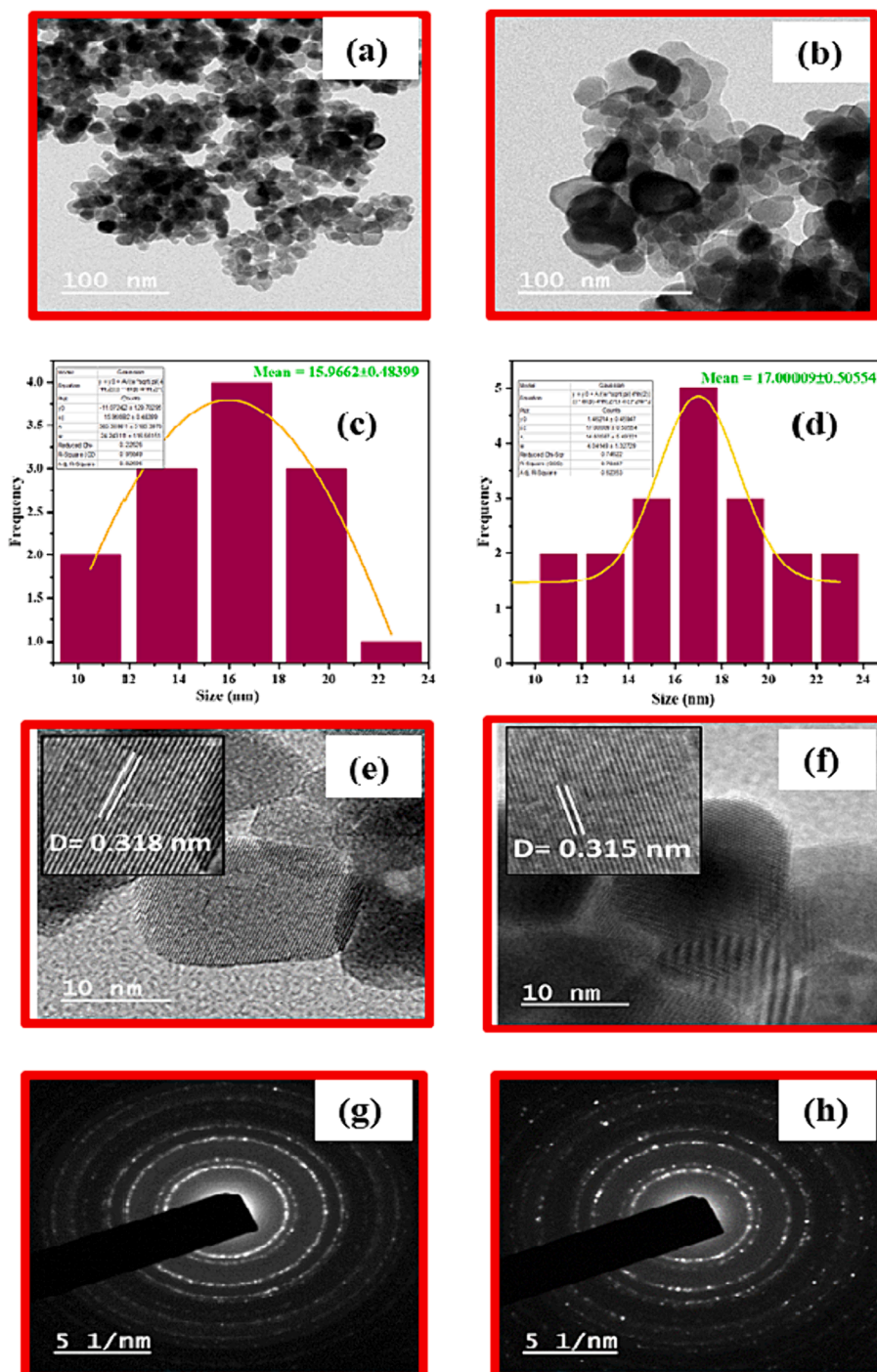
Fig. 11. (a,b) TEM images, (c,d) particle size, (e,f) lattice fringe, (g,h) SAED pattern of CeO$_2$ NPs by sol–gel and hydrothermal method.

holes react with water and generate OH$^{\cdot}$ radicals. The formation of holes and electrons in the valence band and conduction band plays a significant role in the degradation of the dye under sunlight [55,56,57]. The mechanism of photocatalysis using semiconductors is attributed to the oxidative stress induced by Oxidative Reactive Species (ORS) such as superoxide radicals O$_2$, hydroxyl radical OH$^{\cdot}$ and h$^+$[58] The complete photocatalytic reaction of the CeO$_2$ NPs and the MB dye could be written as follows.

$$CeO_2 + h\vartheta \rightarrow CeO_2(e^-_{CB} + h^+_{VB}) \tag{8}$$

$$h^+_{VB} + H_2O \rightarrow H^+ + OH^{\cdot} \tag{9}$$

$$MB + OH^{\cdot} \rightarrow H_2O + CO_2 + mineral\,acid \tag{10}$$

$$e^-_{CB} + O_2 + CO_2 \tag{11}$$

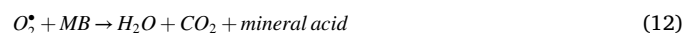$$O^{\bullet}_2 + MB \rightarrow H_2O + CO_2 + mineral\,acid \tag{12}$$
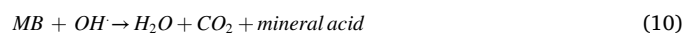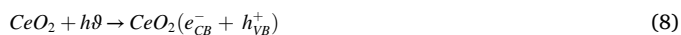
Fig. 13 depicts the position of valence band and conduction band as well as redox potential various possible process happening at surface of the CeO$_2$ catalyst. It reveals from position the redox potential of species involved in the degradation of MB that potential of VB (CeO$_2$) is more positive redox potential of the species and potential of CB (CeO$_2$) is more negative than redox potential of species[60]. Product of the degradation
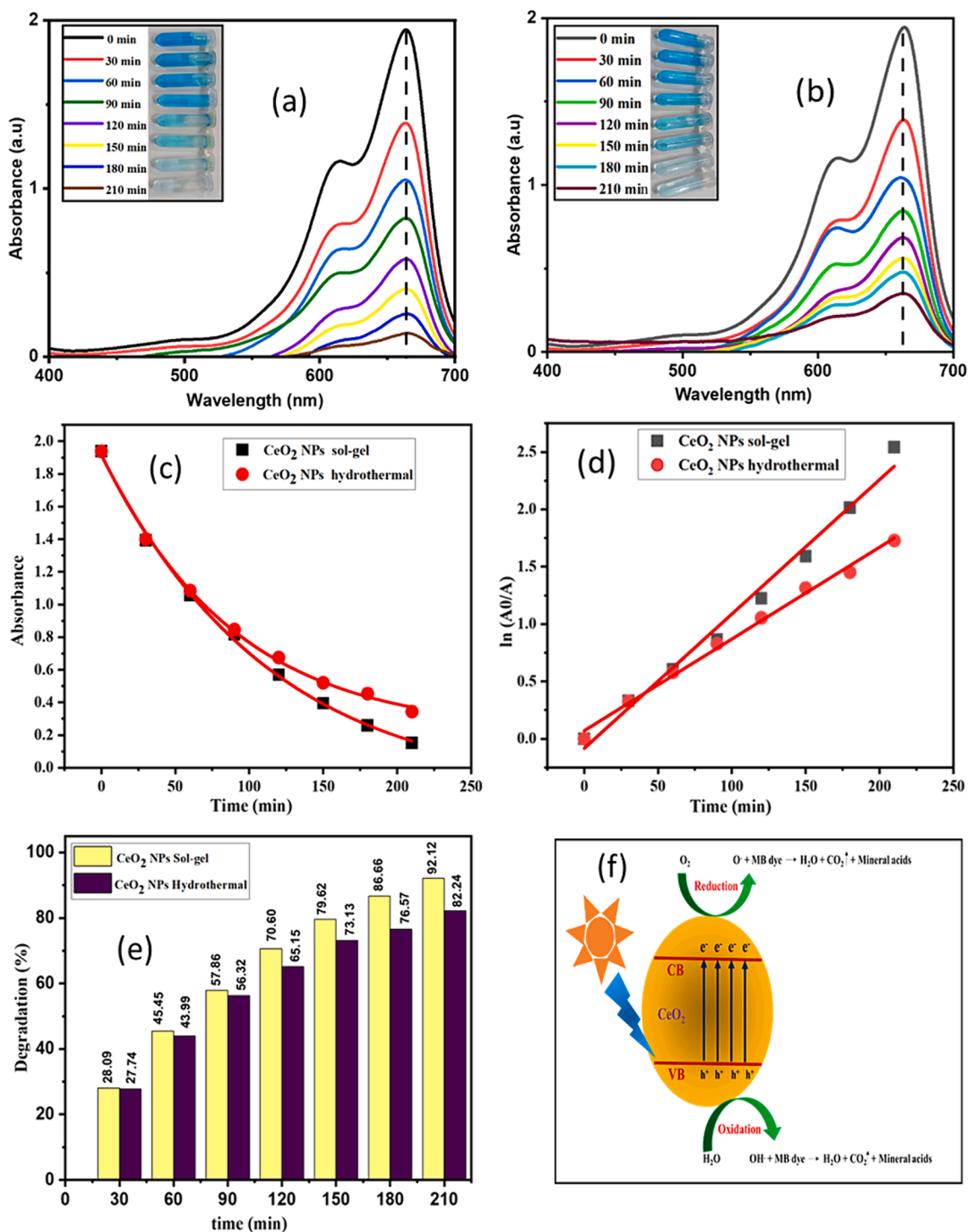
Fig. 12. (a,b) absorption spectra of MB dye degradation catalyzed by CeO_2 NPs by sol–gel and hydrothermal method, (c) absorbance, (d) $\ln(A_0/A)$ versus the irradiation time for sol–gel and hydrothermal method of MB, (e) degradation (%) of MB dye for sol–gel and hydrothermal method, (f) schematic diagram showing the photocatalytic mechanism of synthesized CeO_2 NPs.

are H_2O, CO_2 and mineral acids [59].

3.9.2. Kinetic studies

Fig. 12(c) showed a decrease in the absorbance of dye over time. A simplified Langmuir-Hinshelwood (L-H) kinetic model was used to describe the photocatalytic degradation rate of MB [21].

The reaction kinetic may be expressed by the following equation

$$\ln(A_0/A) = K_r\, t \qquad (13)$$

Where, K_r is a constant rate of reaction, A_0 is the initial concentration of MB, A is the final concentration of MB at time t in min.

The kinetics of the reaction were investigated by logarithm of concentration ratio (A_0/A) versus the irradiation time plot shown Fig. 12(d) by sol–gel and hydrothermal method [22 61]. From the linear fitting curves of $\ln(A_0/A)$ vs irradiation time t, the MB degradation rate constant (k_r) has been calculated as by sol–gel method is 0.010686 min^{-1} and hydrothermal method 0.009077 min^{-1}. sol–gel has the highest
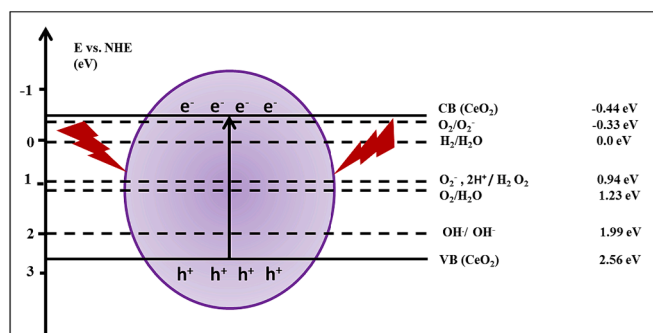
Fig. 13. Band position (valence band top and conduction band bottom) of cerium dioxide (CeO$_2$) compared with several selected redox potentials of processes occurring at the semiconductor surface[59].

degradation rate than the hydrothermal method. Fig. 12(e) degradation (%) of MB dye for sol–gel 92 % and hydrothermal method 82 %. Table 2 shows comparison of present investigation and reported studies of various CeO$_2$ based NPs.

3.10. Gas sensing properties of CeO$_2$ NPs

Fig. 14(a,b) shows the gas response of CeO$_2$ NPs by sol–gel and hydrothermal method to various gases such as ethanol, methanol, CO$_2$, LPG, H$_2$S, and NH$_3$ at different operating temperatures ranging from room temperature (RT) to 350 °C [66]. It showed maximum response to NH$_3$ gas at 200 °C for material synthesized by sol–gel with better response than material synthesized by hydrothermal method.Fig. 15..

Fig. 14(c) shows the selectivity profile of CeO$_2$ NPs by sol–gel and hydrothermal method which indicated that the sensor exhibited higher response to NH$_3$ against other tested gases. It means it is highly selective to NH$_3$ at gas concentration of 100 ppm. From comparing to two methods of preparation, sensor prepared from sol-gel technique showed maximum response to NH$_3$ gas at 200 °C at 100 ppm gas concentrations which was the response found to be 92.34 and for hydrothermal method gas response was 68.71. The NH$_3$ shows better sensing performance because of the lone unshared pair of electrons in the NH$_3$ molecule whereas, ethanol, methanol, CO$_2$, LPG, and H$_2$S don't have unpaired electrons [35]. Therefore, a decrease in the sensing resistance is more with exposure to NH$_3$ gas in comparison with the other target gases.

The response of CeO$_2$ NPs to NH$_3$ gas concentration, as depicted in Fig. 14(d), was investigated employing both sol–gel and hydrothermal methods at an operating temperature of 200 °C. As the concentration of NH$_3$ gas varied from 10 to 140 ppm, it was observed that the response value increased for all samples until it reached 100 ppm at 200 °C. Beyond this concentration, the rate of response increase entered a saturation phase. This behavior can be elucidated by considering that at lower gas concentrations, there were sample sensing sites available on the surface of the films[67]. However, as the gas concentration increased, the surface coverage of gas molecules reached saturation levels, limiting the availability of additional sensing sites. Consequently, this led to a plateau in gas sensitivity[68]. In essence, the active sensing region of the sensor was determined to be around 100 ppm. The gas response for the sol–gel method was measured at 92.98, while for the

hydrothermal method, it was 68.79 [35].

The duration it takes for a sensor to achieve 90 % of the maximum alteration in its resistance when exposed to the target gas is termed as the response time [69]. Conversely, the period needed for the sensor to restore 90 % of its initial resistance is referred to as the recovery time of the sensor. In Fig. 14(e) The CeO$_2$ NPs by sol–gel method has a response time of 31 sec. and a recovery time of 18 sec. and fig.16 (f) hydrothermal method response time is 32 sec. and recovery time 21 sec. n-type semiconductors with outstanding gas-sensing properties. The conductivity of the metal oxide changes due to the adsorption or desorption of a gas on the surface of the substance [70].

#### 3.10.1. Gas sensing mechanism

Based on our previous research, the enhanced gas sensing capabilities of CeO$_2$ nanoparticles synthesized through the sol–gel and hydrothermal methods can be attributed to their reduced particle size, abundant oxygen vacancies, and porous structure. In our investigation, we observed a sequential reaction between NH$_3$ and oxygen species, beginning with the adsorption of oxygen onto the material's surface. Subsequently, the absorbed oxygen captured free electrons, leading to the formation of oxygen anions [35].

$$O_{2(air)} \rightarrow O_{2(ads)} \tag{14}$$

$$O_{2(ads)} + e \rightarrow O_2^- \tag{15}$$

$$O_{2(ads)} + 2e \rightarrow 2O^- \tag{16}$$

$$O_{2(ads)} + 4e \rightarrow 2O^{2-} \tag{17}$$

Two NH$_3$ gas sensing mechanisms were identified in our study. The first mechanism involves the interaction between adsorbed –H$_2$O and NH$_3$ molecules with H$_2$O molecules adsorbed on the CeO$_2$ nanoparticles' surface. This interaction leads to the generation of NH$_4^+$ and OH$^-$, resulting in a reduction in electrical resistance[71]. This process can be described by the following equations [35].

$$NH_{3(gas)} \rightarrow NH_{3(ads)} \tag{18}$$

$$NH_{3(ads)} + H_2O \rightleftarrows NH_4^+ + OH^- \tag{19}$$

Another is pertinent to adsorbed O$^-$. As electron-donating NH$_3$ gas was adsorbed, electrons were then released into the conduction band of the CeO$_2$ nanoparticles as the following equation [12].

$$4NH_{3(ads)} + 3O_{2(ads)}^- \rightarrow 2N_2 + 6H_2O + 3e^- \tag{20}$$
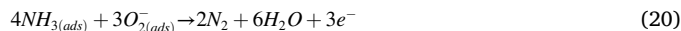
The interaction of gas molecule on the surface of sensing material leads to the release of electron into the conduction band of CeO$_2$ which results in a reduction in electrical resistance. and there after transformation back to metal oxides in the recovery process by heating the sensor to a relatively higher temperature at 450 °C which results recovery to metal oxide [72].

4. Conclusion

In this investigation, CeO$_2$ NPs were synthesized using both sol–gel

Table 2
Comparison of present investigation and reported studies of various CeO$_2$ based NPs.

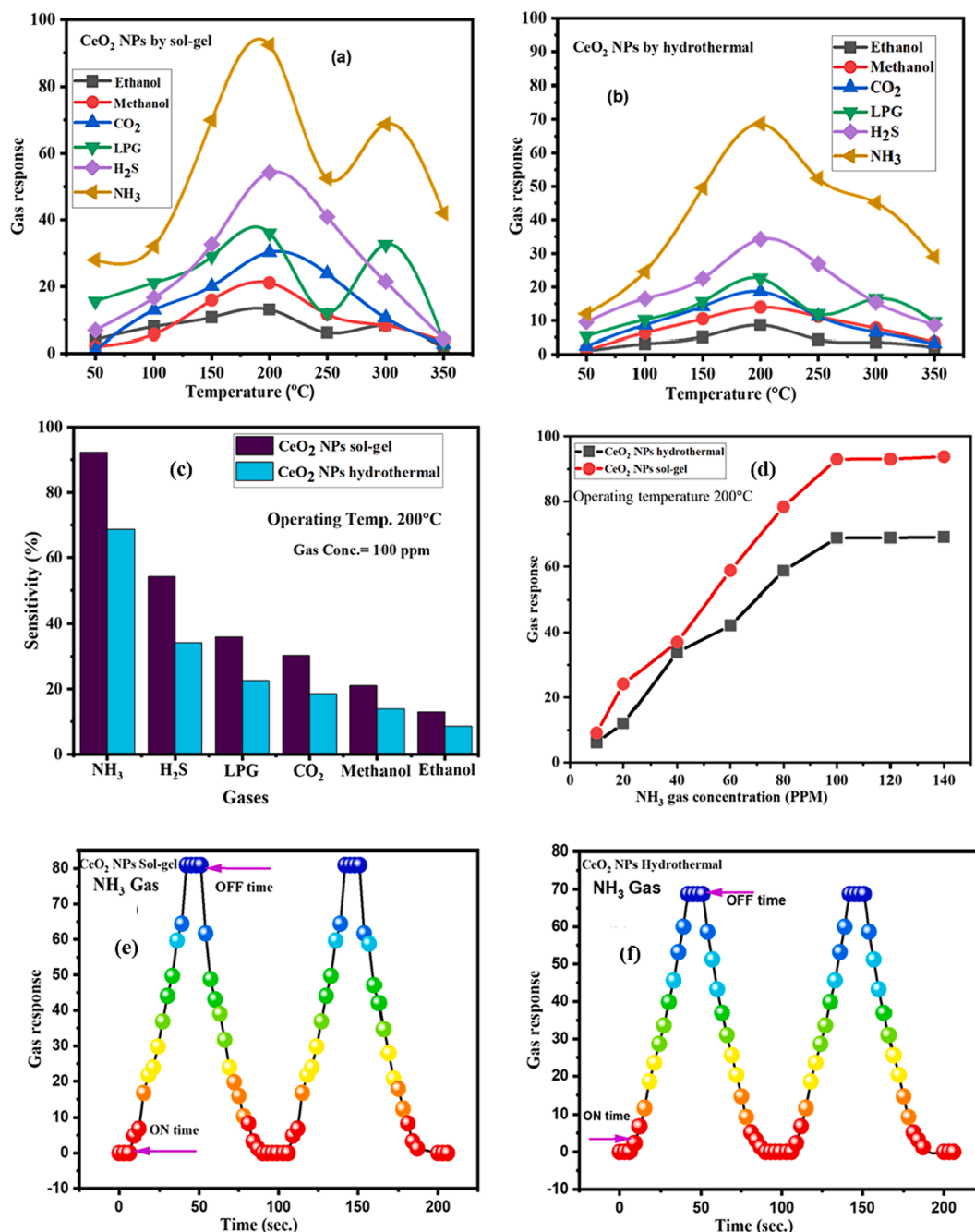| Catalyst	Dye	Synthesis method	Catalyst concentration	Dye concentration	Time duration (min)	Efficiency (%)	References
CeO$_2$	MB	combustion method	50 mg	5 ppm	210	95	[62]
CeO$_2$	MB	co-precipitation method	0.6 mg/L	10 mg/L	240	76	[63]
CeO$_2$	MB	biosynthesis method	1 g L^{-1}	60 mg L^{-1}	180	93	[64]
CeO$_2$	MB	combustion method	100 mg	5 ppm	180	86	[65]
CeO$_2$	MB	Hydrothermal method	10 mg	10 ppm	210	82.24	Present work
CeO$_2$	MB	Sol-gel method	10 mg	10 ppm	210	92.12	Present work

Fig. 14. Gas response of CeO$_2$ NPs by (a) sol–gel and (b) hydrothermal method for various gases at different operating temperatures, (c) Selectivity of CeO$_2$ NPs for sol–gel and hydrothermal method NH$_3$ against other gases, (d) Variation in NH$_3$ gas response with ppm concentration of sol–gel and hydrothermal method, Response and recovery time of CeO$_2$ NPs by (e) sol–gel and (f) hydrothermal method for NH$_3$ gas.

and hydrothermal methods and thoroughly characterized with the help of range of analytical techniques including UV–Vis spectroscopy, FTIR, XRD, Raman spectroscopy, CV, PL spectroscopy, FESEM-EDAX, and TEM-SAED. Regarding photocatalytic performance, the synthesized CeO$_2$ NPs demonstrated significant degradation of methylene blue under natural sunlight. Specifically, the sol–gel method yielded a degradation efficiency of 92 %, surpassing the 82 % achieved with the hydrothermal method over a 210 min. Additionally, gas sensing properties of the CeO$_2$ NPs were evaluated across various gases such as ethanol, methanol, CO$_2$, LPG, H$_2$S, and NH$_3$. Notably, NH$_3$ exhibited the highest response. However, when comparing the sensing performance between the two synthesis methods, CeO$_2$ NPs synthesized via the sol-–gel method outperformed those synthesized via the hydrothermal

method, showcasing superior gas sensing capabilities. In summary, CeO$_2$ NPs synthesized through the sol–gel method exhibited outstanding gas sensing response and photocatalytic activity compared to those synthesized through the hydrothermal method. This underscores the potential superiority of the sol–gel synthesis route for applications in gas sensing and environmental remediation.

CRediT authorship contribution statement

Laxmi D. Sonawane: Writing – original draft, Methodology, Investigation, Data curation, Conceptualization. **Abhinay S. Mandawade:** Data curation. **Laxman N. Bhoye:** Data Curation, Visualization. **Huda I. Ahemad:** Software, Formal analysis. **Swapnil S. Tayade:** Writing –
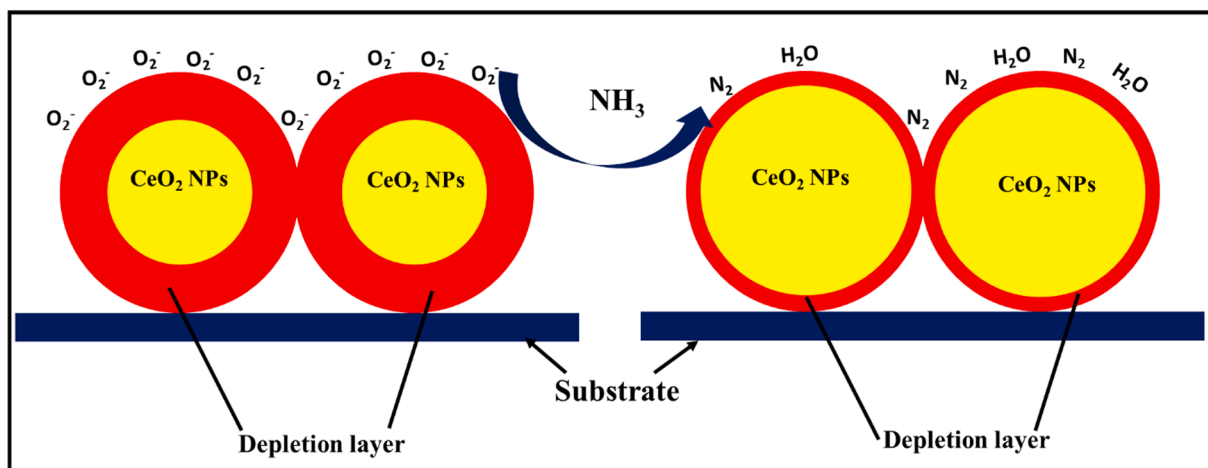
Fig. 15. Schematic diagram of the mechanism of NH₃ gas sensing.

review & editing. **Yogesh B. Aher:** Methodology. **Anil B. Gite:** Methodology, Formal analysis, Data curation. **Latesh K. Nikam:** Data curation. **Sarika D. Shinde:** Methodology. **Gotan H. Jain:** Validation, Methodology. **Ganesh E. Patil:** Supervision, Methodology. **Mahendra S. Shinde:** .

Declaration of competing interest

The authors declare that they have no known competing financial interests or personal relationships that could have appeared to influence the work reported in this paper.

Data availability

Data will be made available on request.

Acknowledgment

References

[1] H.E. Ahmed, Y. Iqbal, M.H. Aziz, M. Atif, Z. Batool, A. Hanif, N. Yaqub, W. A. Farooq, S. Ahmad, A. Fatehmulla, H. Ahmad, Green synthesis of CeO2 nanoparticles from the abelmoschus esculentus extract: evaluation of antioxidant, anticancer, antibacterial, and wound-healing activities, Molecules 26 (2021), https://doi.org/10.3390/molecules26154659.

[2] F. Charbgoo, M. Ramezani, M. Darroudi, Bio-sensing applications of cerium oxide nanoparticles: advantages and disadvantages, Biosens Bioelectron 96 (2017) 33–43, https://doi.org/10.1016/j.bios.2017.04.037.

[3] O.L. Pop, A. Mesaros, D.C. Vodnar, R. Suharoschi, F. Tăbăran, L. Mageruşan, I. S. Tódor, Z. Diaconeasa, A. Balint, L. Ciontea, C. Socaciu, Cerium oxide nanoparticles and their efficient antibacterial application in vitro against gram-positive and gram-negative pathogens, Nanomaterials 10 (2020) 1–15, https://doi.org/10.3390/nano10081614.

[4] A.K. Al-Mousoi, M.K.A. Mohammed, R. Pandey, J. Madan, D. Dastan, G. Ravi, P. Sakthivel, G., Anandha babu, simulation and analysis of lead-free perovskite solar cells incorporating cerium oxide as electron transporting layer, RSC Adv 12 (2022) 32365–32373, https://doi.org/10.1039/d2ra05957f.

[5] D.D. Thiruvoth, M. Ananthkumar, Evaluation of cerium oxide nanoparticle coating as corrosion inhibitor for mild steel, in: Mater Today Proc, Elsevier Ltd, 2021: pp. 2007–2012. https://doi.org/10.1016/j.matpr.2021.08.157.

[6] W. Zhang, N. Zhao, Y. Liu, B. Li, Interconnected CeO2Nanofibers for enhanced CO gas sensing, J Sens 2022 (2022), https://doi.org/10.1155/2022/3097440.

[7] S. Choudhary, K. Sahu, A. Bisht, R. Singhal, S. Mohapatra, Template-free and surfactant-free synthesis of CeO2 nanodiscs with enhanced photocatalytic activity, Appl Surf Sci 503 (2020), https://doi.org/10.1016/j.apsusc.2019.144102.

[8] B. Talluri, K. Yoo, J. Kim, Novel rhombus-shaped cerium oxide sheets as a highly durable methanol oxidation electrocatalyst and high-performance supercapacitor

[9] Y. Temerk, H. Ibrahim, A new sensor based on in doped CeO2 nanoparticles modified glassy carbon paste electrode for sensitive determination of uric acid in biological fluids, Sens Actuators B Chem 224 (2016) 868–877, https://doi.org/10.1016/j.snb.2015.11.029.

[10] G. Murugadoss, D.D. Kumar, M.R. Kumar, N. Venkatesh, P. Sakthivel, Silver decorated CeO2 nanoparticles for rapid photocatalytic degradation of textile rose bengal dye, Sci Rep 11 (2021), https://doi.org/10.1038/s41598-020-79993-6.

[11] F. Wei, C.J. Neal, T.S. Sakthivel, Y. Fu, M. Omer, A. Adhikary, S. Ward, K.M. Ta, S. Moxon, M. Molinari, J. Asiatico, M. Kinzel, S.N. Yarmolenko, V. San Cheong, N. Orlovskaya, R. Ghosh, S. Seal, M. Coathup, A novel approach for the prevention of ionizing radiation-induced bone loss using a designer multifunctional cerium oxide nanozyme, Bioact Mater 21 (2023) 547–565, https://doi.org/10.1016/j.bioactmat.2022.09.011.

[12] P.G. Su, W.Y. Lu, One-pot synthesis of plate-like CeO2 nanosheets for sensing NH3 gas at room temperature, Mater Chem Phys 277 (2022), https://doi.org/10.1016/j.matchemphys.2021.125453.

[13] D.N. Oosthuizen, D.E. Motaung, H.C. Swart, Gas sensors based on CeO2 nanoparticles prepared by chemical precipitation method and their temperature-dependent selectivity towards H2S and NO2 gases, Appl Surf Sci 505 (2020) 144356, https://doi.org/10.1016/j.apsusc.2019.144356.

[14] P. Li, B. Wang, W. Li, C. Qin, L. Sun, N. Wu, Y. Wang, Effect of annealing atmosphere with different oxygen concentration on CO gas sensing performances for CeO2 nanoparticles, Mater Lett 284 (2021) S358–S363, https://doi.org/10.1016/j.matlet.2020.129000.

[15] D. Van Dao, T.T.D. Nguyen, S.M. Majhi, G. Adilbish, H.J. Lee, Y.T. Yu, I.H. Lee, Ionic liquid-supported synthesis of CeO 2 nanoparticles and its enhanced ethanol gas sensing properties, Mater Chem Phys 231 (2019) 1–8, https://doi.org/10.1016/j.matchemphys.2019.03.025.

[16] S. Ata, I. Shaheen, H. Aslam, I.U. Mohsin, N. Alwadai, M. Al Huwayz, M. Iqbal, U. Younas, Barium and strontium doped la-based perovskite synthesis via sol-gel route and photocatalytic activity evaluation for methylene blue, Results Phys 45 (2023), https://doi.org/10.1016/j.rinp.2023.106235.

[17] M. Ishfaq, M. Aadil, S.R. Ejaz, W. Hassan, N.M. Panduro-Tenazoa, M.E. El Sayed, M.N. Murshed, Z.M. El-Bahy, Synthesis of binary metal doped CeO2 via the subcritical hydrothermal method for photo-mineralizing methyl orange dye, J Alloys Compd 960 (2023), https://doi.org/10.1016/j.jallcom.2023.170661.

[18] M.A. Farrukh, K.M. Butt, K. Altaf, S. khadim, Influence of pH and temperature on structural, optical and catalytic investigations of CeO2-SiO2 Nanoparticles, Silicon 11 (2019) 2591–2598, https://doi.org/10.1007/s12633-018-0050-7.

[19] A. Muthuvel, M. Jothibas, V. Mohana, C. Manoharan, Green synthesis of cerium oxide nanoparticles using Calotropis procera flower extract and their photocatalytic degradation and antibacterial activity, Inorg Chem Commun 119 (2020) 108086, https://doi.org/10.1016/j.inoche.2020.108086.

[20] A. Iqbal, A.S. Ahmed, N. Ahmad, A. Shafi, T.Z. Khan, S. Srivastava, Biogenic synthesis of CeO2 nanoparticles and its potential application as an efficient photocatalyst for the degradation of toxic amido black dye, Environ Nanotechnol Monit Manag 16 (2021) 100505, https://doi.org/10.1016/j.enmm.2021.100505.

[21] B. Elahi, M. Mirzaee, M. Darroudi, R. Kazemi Oskuee, K. Sadri, M.S. Amiri, Preparation of cerium oxide nanoparticles in Salvia macrosiphon boiss seeds extract and investigation of their photo-catalytic activities, Ceram Int 45 (2019) 4790–4797, https://doi.org/10.1016/j.ceramint.2018.11.173.

[22] S.R. Ali, R. Kumar, S.K. Kadabinakatti, M.C. Arya, Enhanced UV and visible light - driven photocatalytic degradation of tartrazine by nickel-doped cerium oxide nanoparticles, Mater Res Express 6 (2019), https://doi.org/10.1088/2053-1591/aaee44.

[23] O.P. Moreno, R.G. Pérez, R.P. Merino, M.C. Portillo, G.H. Tellez, E.R. Rosas, M. Z. Tototzintle, CeO2 nanoparticles growth by chemical bath and its thermal

electrode material, Ceram Int 48 (2022) 164–172, https://doi.org/10.1016/j.ceramint.2021.09.092.

annealing treatment in air atmosphere, Optik (stuttg) 148 (2017) 142–150, https://doi.org/10.1016/j.ijleo.2017.08.133.

[24] P. Periyat, F. Laffir, S.A.M. Tofail, E. Magner, A facile aqueous sol-gel method for high surface area nanocrystalline CeO 2, RSC Adv 1 (2011) 1794–1798, https://doi.org/10.1039/c1ra00524c.

[25] J. Zdravković, B. Simović, A. Golubović, D. Poleti, I. Veljković, M. Šćepanović, G. Branković, Comparative study of CeO2 nanopowders obtained by the hydrothermal method from various precursors, Ceram Int 41 (2015) 1970–1979, https://doi.org/10.1016/j.ceramint.2014.08.122.

[26] R. Suresh, V. Ponnuswamy, R. Mariappan, N. Senthil Kumar, Influence of substrate temperature on the properties of CeO2 thin films by simple nebulizer spray pyrolysis technique, Ceram Int 40 (2014) 437–445, https://doi.org/10.1016/j.ceramint.2013.06.020.

[27] Z. Li, B. Hou, Y. Xu, D. Wu, Y. Sun, W. Hu, F. Deng, Comparative study of sol-gel-hydrothermal and sol-gel synthesis of titania-silica composite nanoparticles, J Solid State Chem 178 (2005) 1395–1405, https://doi.org/10.1016/j.jssc.2004.12.034.

[28] E.I. Seck, J.M. Doña-Rodríguez, E. Pulido Melián, C. Fernández-Rodríguez, O. M. González-Díaz, D. Portillo-Carrizo, J. Pérez-Peña, Comparative study of nanocrystalline titanium dioxide obtained through sol-gel and sol-gel-hydrothermal synthesis, J Colloid Interface Sci 400 (2013) 31–40, https://doi.org/10.1016/j.jcis.2013.03.019.

[29] M. Bilton, S.J. Milne, A.P. Brown, Comparison of hydrothermal and sol-gel synthesis of Nano-Particulate hydroxyapatite by Characterisation at the bulk and Particle level, Open Journal of Inorganic Non-Metallic Materials 02 (2012) 1–10, https://doi.org/10.4236/ojinm.2012.21001.

[30] P. Tamizhdurai, S. Sakthinathan, S.M. Chen, K. Shanthi, S. Sivasanker, P. Sangeetha, Environmentally friendly synthesis of CeO2 nanoparticles for the catalytic oxidation of benzyl alcohol to benzaldehyde and selective detection of nitrite, Sci Rep 7 (2017) 46372, https://doi.org/10.1038/srep46372.

[31] S. Ahmadian-Fard-Fini, D. Ghanbari, M. Salavati-Niasari, Photoluminescence carbon dot as a sensor for detecting of Pseudomonas aeruginosa bacteria: hydrothermal synthesis of magnetic hollow NiFe 2 O 4 -carbon dots nanocomposite material, Compos B Eng 161 (2019) 564–577, https://doi.org/10.1016/j.compositesb.2018.12.131.

[32] M. Panahi-Kalamuei, S. Alizadeh, M. Mousavi-Kamazani, M. Salavati-Niasari, Synthesis and characterization of CeO2 nanoparticles via hydrothermal route, Journal of Industrial and Engineering Chemistry 21 (2015) 1301–1305, https://doi.org/10.1016/j.jiec.2014.05.046.

[33] S. Masoumi, G. Nabiyouni, D. Ghanbari, Photo-degradation of congored, acid brown and acid violet: photo catalyst and magnetic investigation of CuFe2O4–TiO2–Ag nanocomposites, Journal of Materials Science: Materials in Electronics 27 (2016) 11017–11033, https://doi.org/10.1007/s10854-016-5218-6.

[34] S. Safat, F. Buazar, S. Albukhaty, S. Matroodi, Enhanced sunlight photocatalytic activity and biosafety of marine-driven synthesized cerium oxide nanoparticles, Sci Rep 11 (2021) 14734, https://doi.org/10.1038/s41598-021-94327-w.

[35] U.B. Tumberphale, S.S. Jadhav, S.D. Raut, P.V. Shinde, S. Sangle, S.F. Shaikh, A. M. Al-Enizi, M. Ubaidullah, R.S. Mane, S.K. Gore, Tailoring ammonia gas sensing performance of La3+-doped copper cadmium ferrite nanostructures, Solid State Sci 100 (2020), https://doi.org/10.1016/j.solidstatesciences.2019.106089.

[36] M. Behzadi, S. Jarollahi, A.A. Irvani, M. Ghanbarib, Green synthesis and antibacterial activity of silver Nanoparticles using Dracocephalum Moldavica leaves Extract, J Nanostruct 12 (2022) 1059–1066, https://doi.org/10.22052/JNS.2022.04.026.

[37] M. Kurian, C. Kunjachan, Investigation of size dependency on lattice strain of nanoceria particles synthesised by wet chemical methods, Int Nano Lett 4 (2014) 73–80, https://doi.org/10.1007/s40089-014-0122-7.

[38] M.S. Pujar, S.M. Hunagund, D.A. Barretto, V.R. Desai, S. Patil, S.K. Vootla, A. H. Sidarai, Synthesis of cerium-oxide NPs and their surface morphology effect on biological activities, Bulletin of Materials Science 43 (2020), https://doi.org/10.1007/s12034-019-1962-6.

[39] D. Prieur, W. Bonani, K. Popa, O. Walter, K.W. Kriegsman, M.H. Engelhard, X. Guo, R. Eloirdi, T. Gouder, A. Beck, T. Vitova, A.C. Scheinost, K. Kvashnina, P. Martin, Size dependence of lattice Parameter and electronic structure in CeO2 Nanoparticles, Inorg Chem 59 (2020) 5760–5767, https://doi.org/10.1021/acs.inorgchem.0c00506.

[40] F. Meng, H. Li, J. Gong, Z. Fan, Photocatalytic and magnetic properties of loosened ceria hollow microspheres synthesized by a single-step hydrothermal method, Journal of Materials Science: Materials in Electronics 27 (2016) 8433–8439, https://doi.org/10.1007/s10854-016-4857-y.

[41] Z. Zhang, Y. Wang, M. Wang, J. Lü, L. Li, Z. Zhang, M. Li, J. Jiang, F. Wang, An investigation of the effects of CeO2 crystal planes on the aerobic oxidative synthesis of imines from alcohols and amines, cuihua xuebao/chinese, Journal of Catalysis 36 (2015) 1623–1630, https://doi.org/10.1016/S1872-2067(15)60869-5.

[42] V. Pathak, P. Lad, A.B. Thakkar, P. Thakor, M.P. Deshpande, S. Pandya, Synthesis, characterization and applications of cubic fluorite cerium oxide nanoparticles: a comprehensive study, Results in Surfaces and Interfaces 11 (2023) 100111, https://doi.org/10.1016/j.rsurfi.2023.100111.

[43] H. Wang, M. Liang, X. Zhang, D. Duan, W. Shi, Y. Song, Z. Sun, Novel CeO2 nanorod framework prepared by dealloying for supercapacitors applications, Ionics (kiel) 24 (2018) 2063–2072, https://doi.org/10.1007/s11581-018-2443-4.

[44] A. Jeyaranjan, T.S. Sakthivel, M. Molinari, D.C. Sayle, S. Seal, Morphology and crystal planes effects on supercapacitance of CeO2 nanostructures: electrochemical and Molecular dynamics studies, Particle and Particle Systems Characterization 35 (2018) 1800176, https://doi.org/10.1002/ppsc.201800176.

[45] M. Alagar, A. Nadar, J.A. College, N. Ramjeyanthi, M. Alagar, D. Muthuraman, Synthesis, Structural and Optical Behavior of Cerium Oxide Nanoparticles by Co-Precipitation Method, 4 (2018) 44-51. www.ijsrst.com.

[46] D. Quade, S. Jana, L. McCorkle, The influence of thin film adhesives in pullout tests between nickel–titanium shape memory alloy and carbon fiber reinforced polymer matrix composites, Compos B Eng 176 (2019) 107321, https://doi.org/10.1016/j.compositesb.2019.107321.

[47] C. Sudhamani, Cerium oxide Nanoparticles-a green, Reusable, and Highly Efficient Heterogeneous Catalyst for the Synthesis of Polyhydroquinolines under Solvent-Free Conditions 3 (2011) 373–382. https://www.researchgate.net/publication/267783853.

[48] G. Jayakumar, A. Albert Irudayaraj, A. Dhayal Raj, Particle size effect on the properties of cerium oxide (CeO2), Nanoparticles Synthesized by Hydrothermal Method 9 (2017) 2412–5954, https://doi.org/10.2412/mmse.3.4.481.

[49] J. Malleshappa, H. Nagabhushana, B.D. Prasad, S.C. Sharma, Y.S. Vidya, K. S. Anantharaju, Structural, photoluminescence and thermoluminescence properties of CeO2 nanoparticles, Optik (stuttg) 127 (2016) 855–861, https://doi.org/10.1016/j.ijleo.2015.10.114.

[50] M.E. Ioannou, G.K. Pouroutzidou, I. Chatzimentor, I. Tsamesidis, N. Florini, I. Tsiaoussis, E. Lymperaki, P. Komninou, E. Kontonasaki, Synthesis and Characterization of cerium oxide Nanoparticles: effect of cerium precursor to gelatin ratio, Applied Sciences (switzerland) 13 (2023), https://doi.org/10.3390/app13042676.

[51] G. Jayakumar, A. Albert Irudayaraj, A. Dhayal Raj, A comprehensive investigation on the properties of nanostructured cerium oxide, opt, Quantum Electron 51 (2019), https://doi.org/10.1007/s11082-019-2029-z.

[52] A. Younis, D. Chu, Y.V. Kaneti, S. Li, Tuning the surface oxygen concentration of 111 surrounded ceria nanocrystals for enhanced photocatalytic activities, Nanoscale 8 (2016) 378–387, https://doi.org/10.1039/c5nr06588g.

[53] E. Raudonyte-Svirbutaviciene, A. Neagu, V. Vickackaite, V. Jasulaitiene, A. Zarkov, C.W. Tai, A. Katelnikovas, Two-step photochemical inorganic approach to the synthesis of ag-CeO2 nanoheterostructures and their photocatalytic activity on tributyltin degradation, J Photochem Photobiol A Chem 351 (2018) 29–41, https://doi.org/10.1016/j.jphotochem.2017.10.008.

[54] M.T. Yagub, T.K. Sen, M. Ang, Removal of cationic dye methylene blue (MB) from aqueous solution by ground raw and base modified pine cone powder, environ, Earth Sci 71 (2014) 1507–1519, https://doi.org/10.1007/s12665-013-2555-0.

[55] R. Suresh, K. Giribabu, R. Manigandan, S. Munusamy, S. Praveen Kumar, S. Muthamizh, A. Stephen, V. Narayanan, Doping of co into V2O5 nanoparticles enhances photodegradation of methylene blue, J Alloys Compd 598 (2014) 151–160, https://doi.org/10.1016/j.jallcom.2014.02.041.

[56] R. Saravanan, V.K. Gupta, V. Narayanan, A. Stephen, Comparative study on photocatalytic activity of ZnO prepared by different methods, J Mol Liq 181 (2013) 133–141, https://doi.org/10.1016/j.molliq.2013.02.023.

[57] Z. Ghaedrahmat, S.M. Moussavi, S. Jorfi, M.A. Mohasel, N. Jaafarzadeh, Enhanced photocatalytic degradation of 4-chlorophenol using lanthanum oxide Nano-particles under uVC/Vis irradiation, Journal of Nanostructures 11 (2021) 165–180. https://doi.org/10.22052/JNS.2021.01.018.

[58] Y. Hao, L. Li, J. Zhang, H. Luo, X. Zhang, E. Chen, Multilayer and open structure of dendritic crosslinked CeO2-ZrO2 composite: enhanced photocatalytic degradation and water splitting performance, Int J Hydrogen Energy 42 (2017) 5916–5929, https://doi.org/10.1016/j.ijhydene.2017.01.093.

[59] E. Kusmierek, A CeO2 semiconductor as a photocatalytic and photoelectrocatalytic material for the remediation of pollutants in industrial wastewater: a review, Catalysts 10 (2020) 1–54, https://doi.org/10.3390/catal10121435.

[60] H. Li, Y. Cui, W. Hong, High photocatalytic performance of BiOI/Bi 2 WO 6 toward toluene and reactive brilliant red, Appl Surf Sci 264 (2013) 581–588, https://doi.org/10.1016/j.apsusc.2012.10.068.

[61] S. Fu, Y. Du, J. Bie, Z. Huang, H. Hu, Q. Huang, H. Zhu, W. Yuan, L. Li, B. Liu, Facile fabrication of Z-scheme Ag2WO4/BiOBr heterostructure with oxygen vacancies for improved visible-light photocatalytic performance, Journal of Science: Advanced Materials and Devices 8 (2023), https://doi.org/10.1016/j.jsamd.2023.100561.

[62] S.A. Vinutha, A.M. Meghashree, D.M. Gurudutt, D.S. Kudlur, K.C. Sunil Kumar, G. Karthik, N. Arun Kumar, V. Lakshmi Ranganatha, P. Parameswara, C. Mallikarjunaswamy, Facile green synthesis of cerium oxide nanoparticles using Jacaranda mimosifolia leaf extract and evaluation of their antibacterial and photodegradation activity, in: Mater Today Proc, Elsevier Ltd, 2023: pp. 105–112. https://doi.org/10.1016/j.matpr.2023.05.592.

[63] V. Pathak, P. Lad, A.B. Thakkar, P. Thakor, M.P. Deshpande, S. Pandya, Synthesis, characterization and applications of cubic fluorite cerium oxide nanoparticles: a comprehensive study, Results in Surfaces and Interfaces 11 (2023), https://doi.org/10.1016/j.rsurfi.2023.100111.

[64] D. Moro Druzian, L. Rodrigues Oviedo, S. Nunes Loureiro, R. Dias Wouters, B. Stefanello Vizzotto, E. de Oliveira Pinto, N. Julia Schüssler de Vanconcellos, Y. Patricia Moreno Ruiz, A. Galembeck, G. Pavoski, D. Crocce Romano Espinosa, C. dos Santos, W. Leonardo da Silva, Cerium oxide nanoparticles: Biosynthesis, characterization, antimicrobial, ecotoxicity and photocatalytic activity, J Photochem Photobiol A Chem 442 (2023). https://doi.org/10.1016/j.jphotochem.2023.114773.

[65] L.S. Reddy Yadav, K. Lingaraju, B. Daruka Prasad, C. Kavitha, G. Banuprakash, G. Nagaraju, Synthesis of CeO2 nanoparticles: photocatalytic and antibacterial activities, Eur Phys J plus 132 (2017), https://doi.org/10.1140/epjp/i2017-11462-4.

[66] G. Ramanathan, N. Srinivasan, Arunsankar, K.R. Murali, Detection of H2S gas sensing performance of sol gel prepared metal oxide (In2O3, SnO2, sn doped

In2O3) thin films, Mater Today Proc (2023), https://doi.org/10.1016/j. matpr.2023.05.320.

[67] J. Liu, Y. Chen, T. Lin, D. Lai, T. Wen, C. Sun, J. Juang, [IEEE 2011 Fifth International Conference on Sensing Technology (ICST 2011) - Palmerston North, New Zealand (2011.11.28-2011.12.1)] 2011 Fifth International Conference on Sensing Technology - Developed urban air quality monitoring system based on wireless sensor networks 0 (2011) 549–554. doi:10.1109/icsenst.2011.6137040.

[68] M. Yu, X. Liu, Y. Wang, Y. Zheng, J. Zhang, M. Li, W. Lan, Q. Su, Gas sensing properties of p-type semiconducting vanadium oxide nanotubes, Appl Surf Sci 258 (2012) 9554–9558, https://doi.org/10.1016/j.apsusc.2012.05.120.

[69] G.E. Patil, D.D. Kajale, D.N. Chavan, N.K. Pawar, P.T. Ahire, S.D. Shinde, V. B. Gaikwad, G.H. Jain, Synthesis, characterization and gas sensing performance of SnO 2 thin films prepared by spray pyrolysis, Bull. Mater. Sci 34 (2011) 1–9, https://doi.org/10.1007/s12034-011-0045-0.

[70] S.D. Shinde, G.E. Patil, D.D. Kajale, V.B. Gaikwad, G.H. Jain, Synthesis of ZnO nanorods by spray pyrolysis for H 2S gas sensor, J Alloys Compd 528 (2012) 109–114, https://doi.org/10.1016/j.jallcom.2012.03.020.

[71] K. Schneider, M. Lubecka, A. Czapla, V2O5 thin films for gas sensor applications, Sens Actuators B Chem 236 (2016) 970–977, https://doi.org/10.1016/j. snb.2016.04.059.

[72] Z. Li, H. Li, Z. Wu, M. Wang, J. Luo, H. Torun, P. Hu, C. Yang, M. Grundmann, X. Liu, Y. Fu, Advances in designs and mechanisms of semiconducting metal oxide nanostructures for high-precision gas sensors operated at room temperature, Mater Horiz 6 (2019) 470–506, https://doi.org/10.1039/c8mh01365a.

Dr. Mahendra Shantaram Shinde is The Assistant Professor and Head at Department of Physics, M.J.M. Arts, Commerce & Science College, Karanjali (Peth), Dist.-Nashik - 422 208(M. S.) India. He received his Ph.D. in Materials Science. He has been teaching physics for UG students since last 11 years. He has completed his MSc (Physics) from Savitribai Phule Pune University, Pune. He has completed his Ph.D from North Maharashtra University, Jalgaon (MH). He has been Recognized as Ph. D and M.Phil. Supervisor (Guide) and P.G. Recognized Teacher by S. P. P. U, Pune (Maharashtra), India. He has published 23-research papers in reputed National/International journals and also published 10-text books 4-reference books. He reviewed research papers for reputed international journals. He work as Ph.D. thesis referee. His topics of research interest are Thin films, Nanomaterials, gas sensors, photoconducting and photo luminescent materials, photo catalytic activity thin film solar cells, properties of nanocrystalline semiconducting thin films.